Supplementary Material for

Temperature-affected nano-deformation behaviors of nanometals in ultrahigh-strain-rate forming processes

Jian Liu [a], Yali He [a], Yaowu Hu [a,b*]

[a] The Institute of Technological Sciences, Wuhan University, Wuhan, 430072, China

[b] School of Power and Mechanical Engineering, Wuhan University, 430072 Wuhan, China
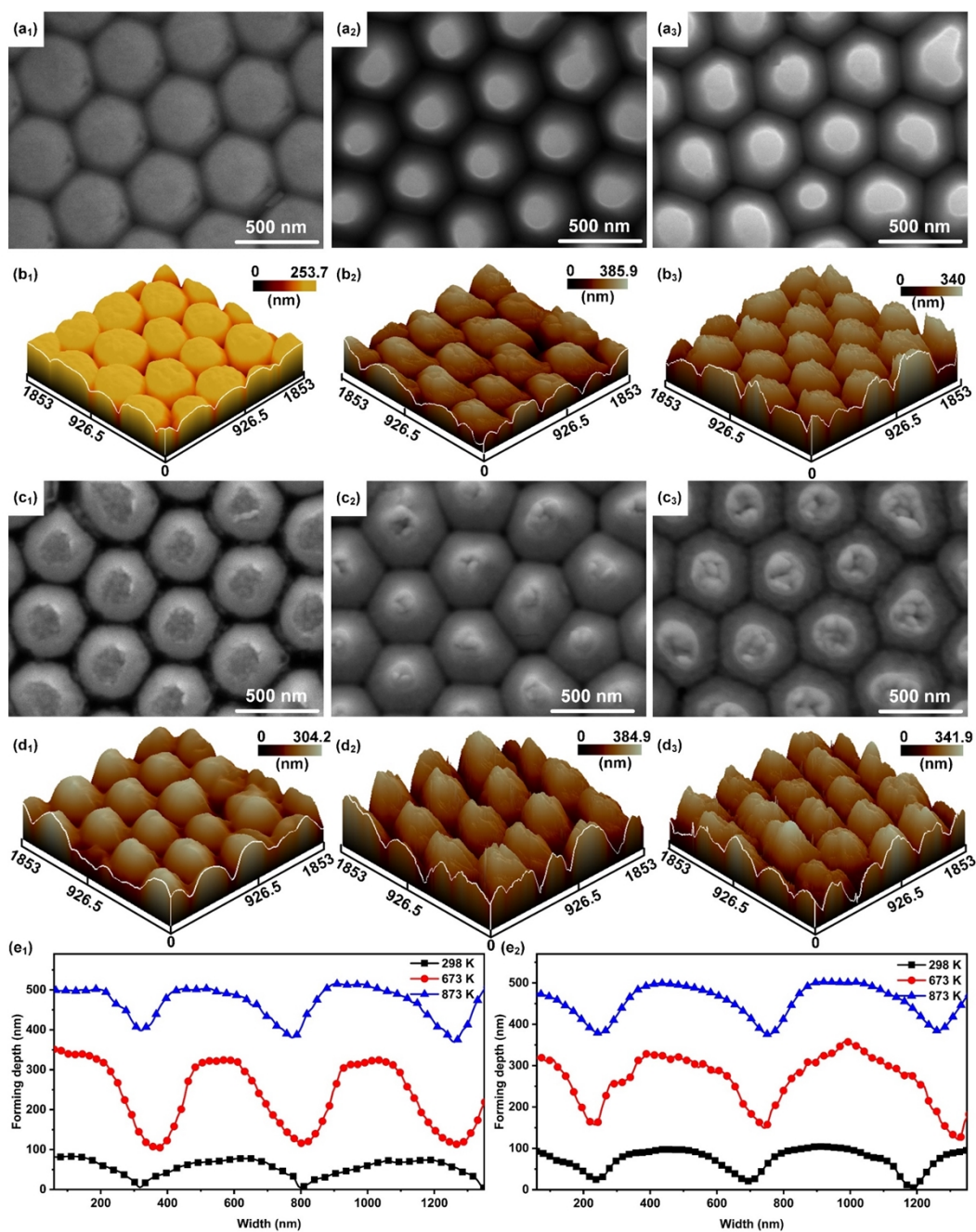
*Corresponding author: Yaowu Hu

E-mail: yaowuhu@whu.edu.cn

This file includes:

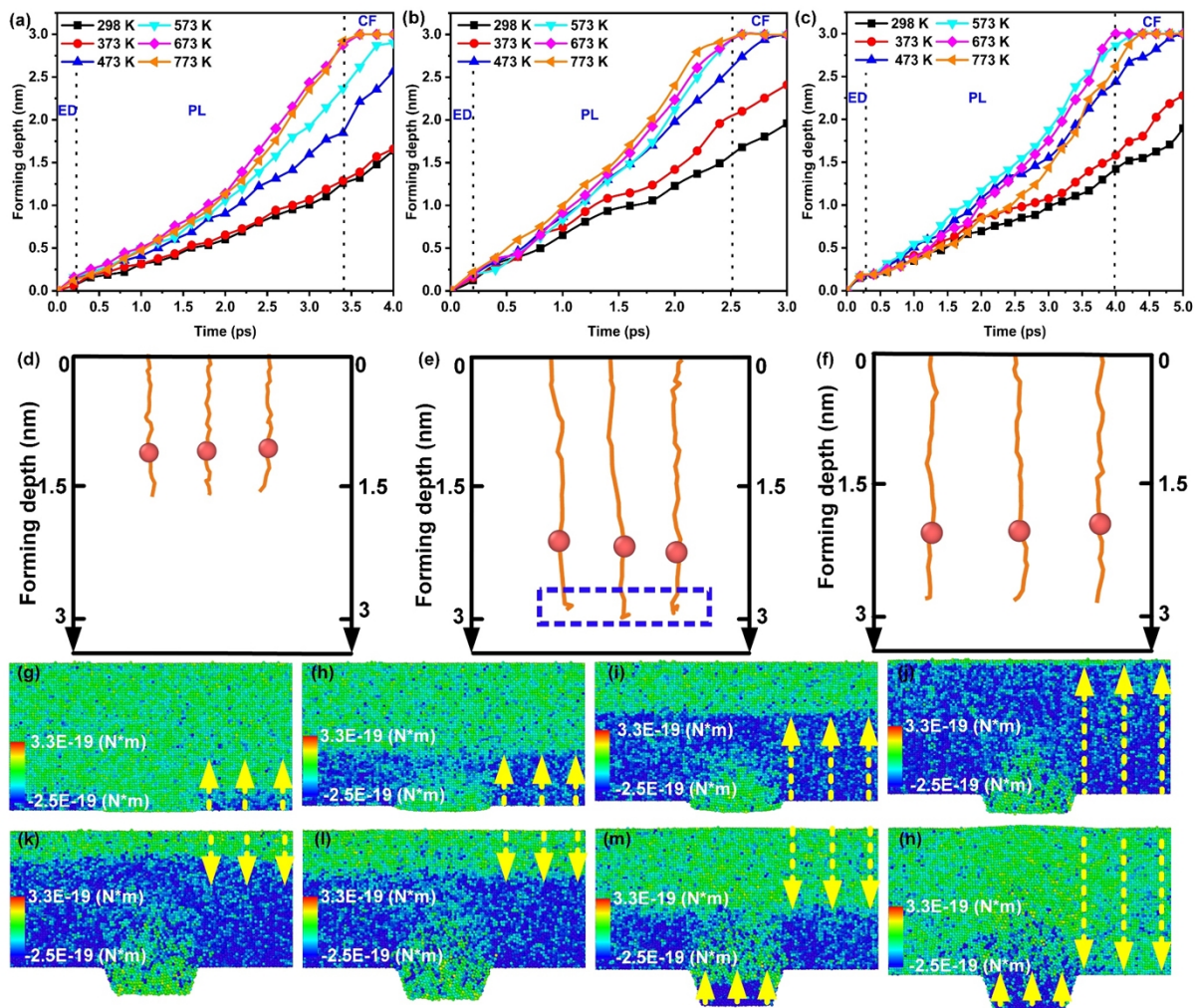Supplementary Figures 1-9

Supplementary Tables 1, 2

Supplementary notes

Supplementary Fig. S1 Morphologies of the Al and Ag nanostructures formed at various temperatures. (a_1–a_3) SEM images of the Al nanostructures formed at 298 K, 773 K, and 873 K, respectively. (b_1–b_3) 3D morphologies of nanostructures in Fig. S1(a_1–a_3). (c_1)-(c_3) SEM images of the Ag nanostructures formed at 298 K, 773 K, and 873 K, respectively. (d_1–d_3) 3D morphologies of the Ag nanostructures in Fig. S1(c_1–c_3). (e_1) and (e_2) 2D profiles of the Al and Ag nanostructures, respectively.
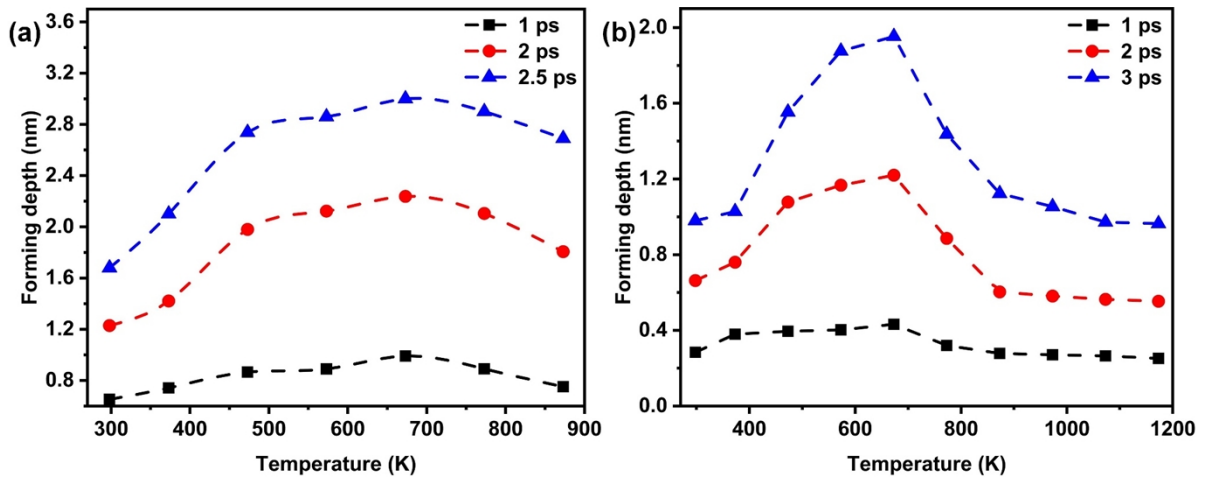
Supplementary Fig. S2 Formation depth of Al and Ag nanostructures. (a) Formation depth of the Al nano-sheet. (b) Formation depth of the Ag nano-sheet..

**Supplementary Fig. S3** Correlation between dynamic deformation behavior and shock wave transmission at ultra-high strain rates. (a–c) Dynamic forming curves of Au, Ag, and Al, respectively. (d–f) Atomic trajectory lines of the Au atoms at 298 K, 673 K, and 873 K, respectively. (g–m) Snapshots of the stress propagation along the z-axis: (d) 0.2 ps, (e) 0.8 ps, (f) 1.2 ps, (g) 1.8 ps, (h) 2.2 ps, (i) 2.5 ps, (j) 2.8 ps, (k) 3.0 ps.
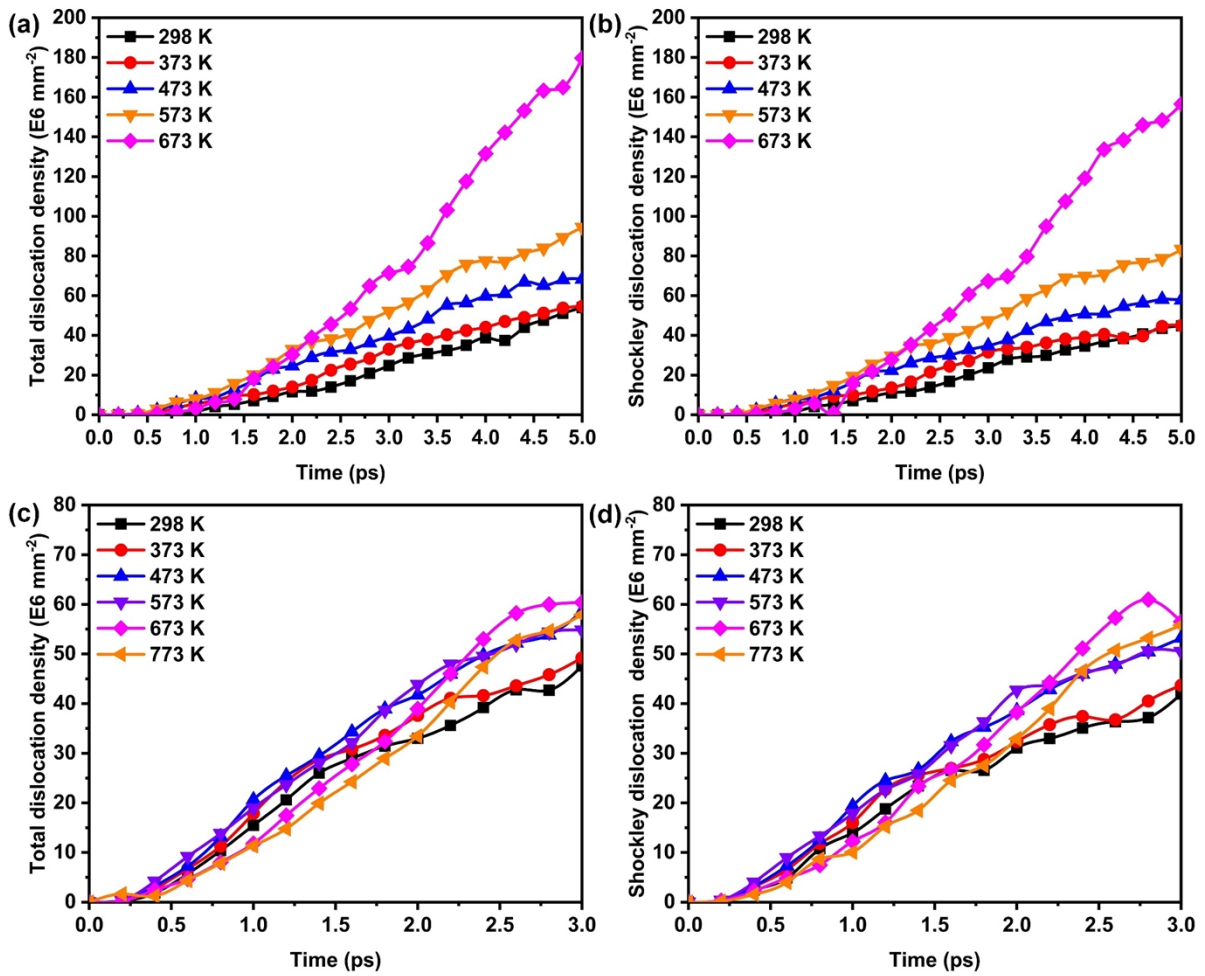
Supplementary Fig. S4 Dynamic dislocation density evolution curves of Al and Ag in thermal-promoted forming stage. (a) Evolution of total dislocation density of Ag. (b) Evolution of Shockley partial dislocation density of Ag. (c) Evolution of total dislocation density of Al. (d) Evolution of Shockley partial dislocation density of Al.
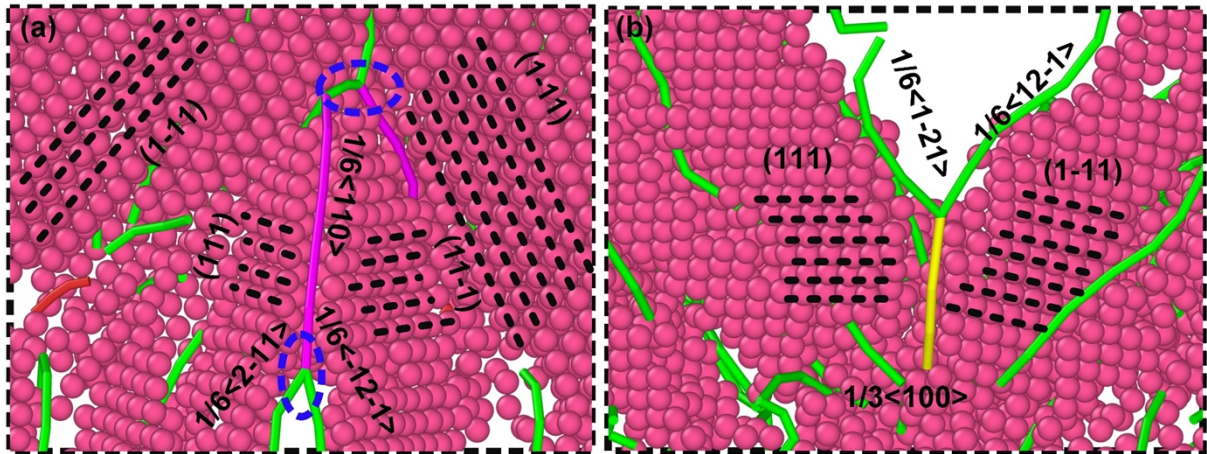
Supplementary Fig. S5 Lomer-Cottrell locks and Hirth locks. (a) Enlarged view of the stair-rod dislocations. (b) Enlarged view of the Hirth block.
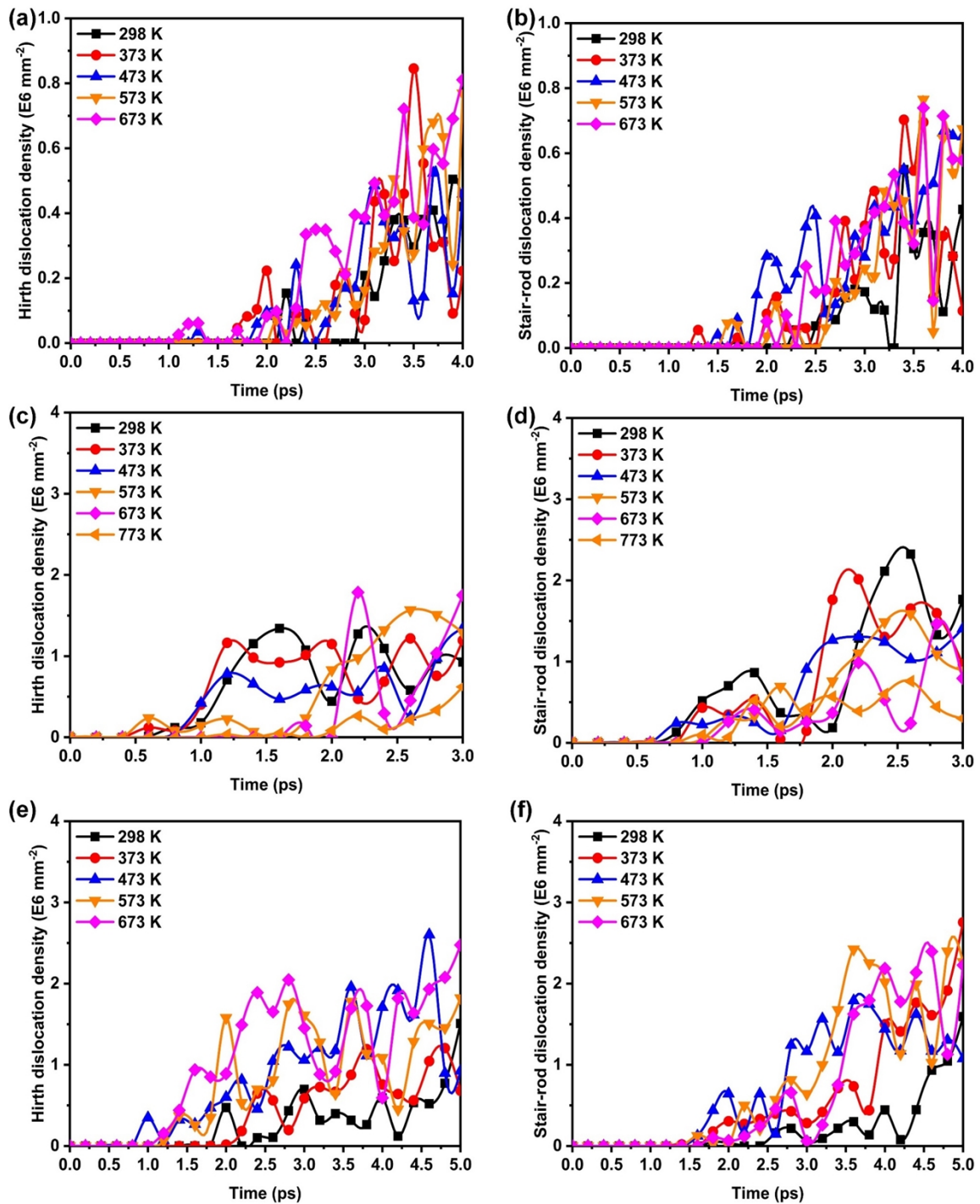
Supplementary Fig. S6 Dynamic evolution curves of hardening dislocations in thermal-promoted forming process: (a) Hirth dislocation density curves of Au. (b) Stair-rod dislocation density curves of Au. (c) Hirth dislocation density curves of Al. (d) Stair-rod dislocation density curves of Al. (e) Hirth dislocation density curves of Ag. (f) Stair-rod dislocation density curves of Ag.
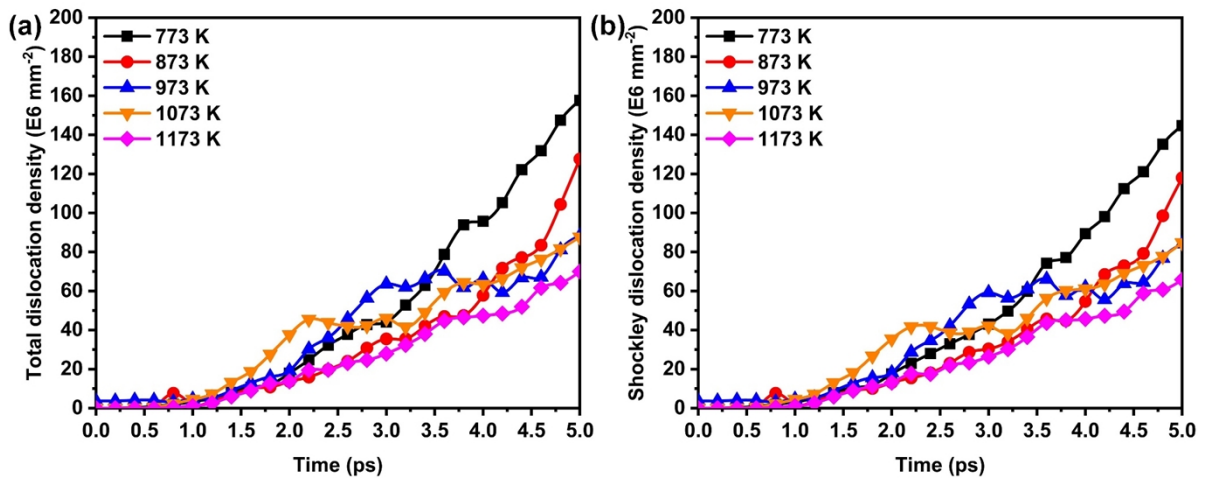
Supplementary Fig. S7 Dislocation evolution curves of Ag in thermal-weakened formability stage. (a) Evolution curves of the total dislocation density. (b) Evolution curves of the Shockley partial dislocation density.
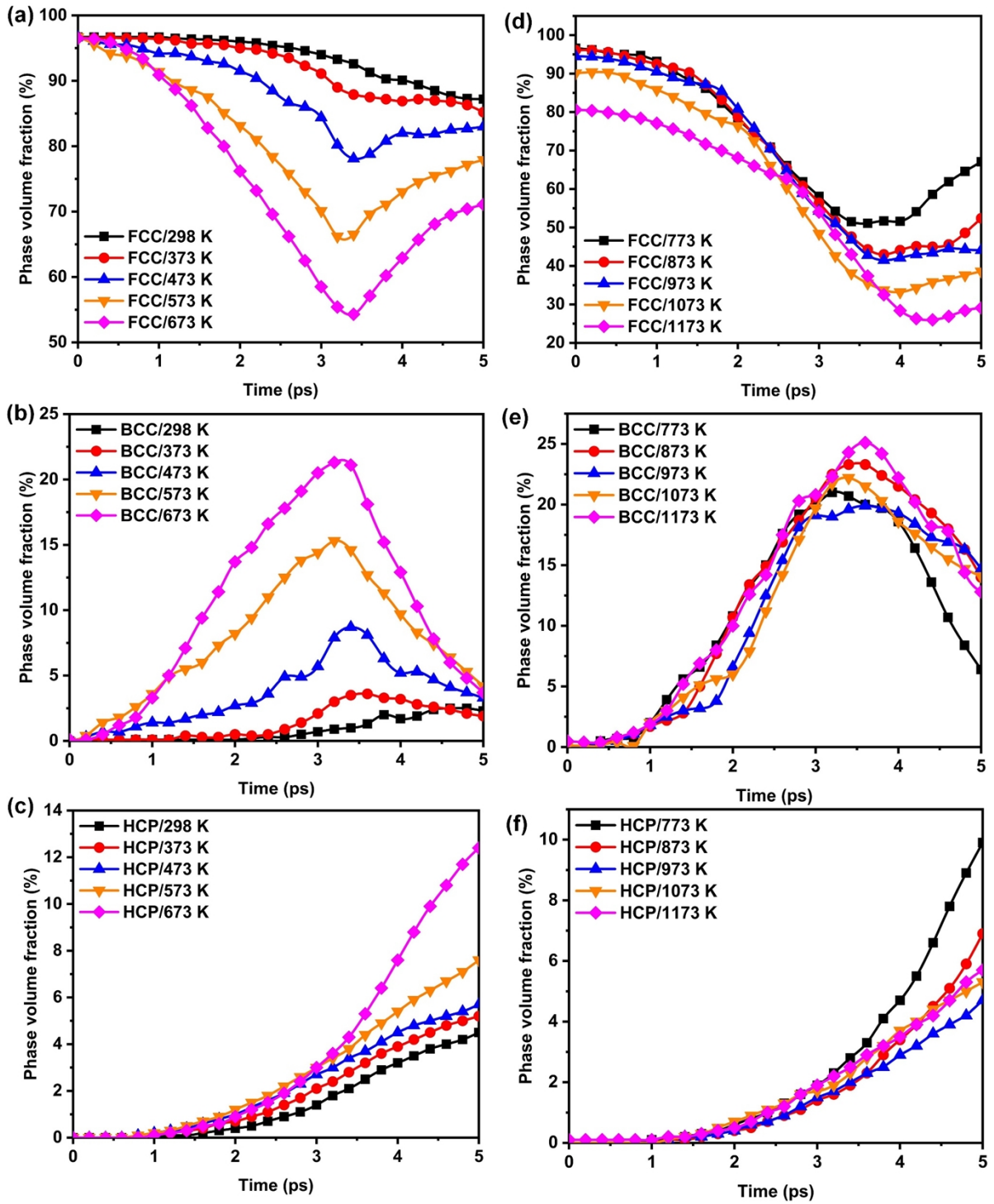
Supplementary Fig. S8 Phase volume fraction evolution of the Ag nanostructures at various temperatures. (a–c) Phase volume fraction curves of FCC, BCC and HCP in thermal-promoted forming stage, respectively. (d–f) Phase volume fraction curves of FCC, BCC and HCP in thermal-weakened forming stage, respectively.

9
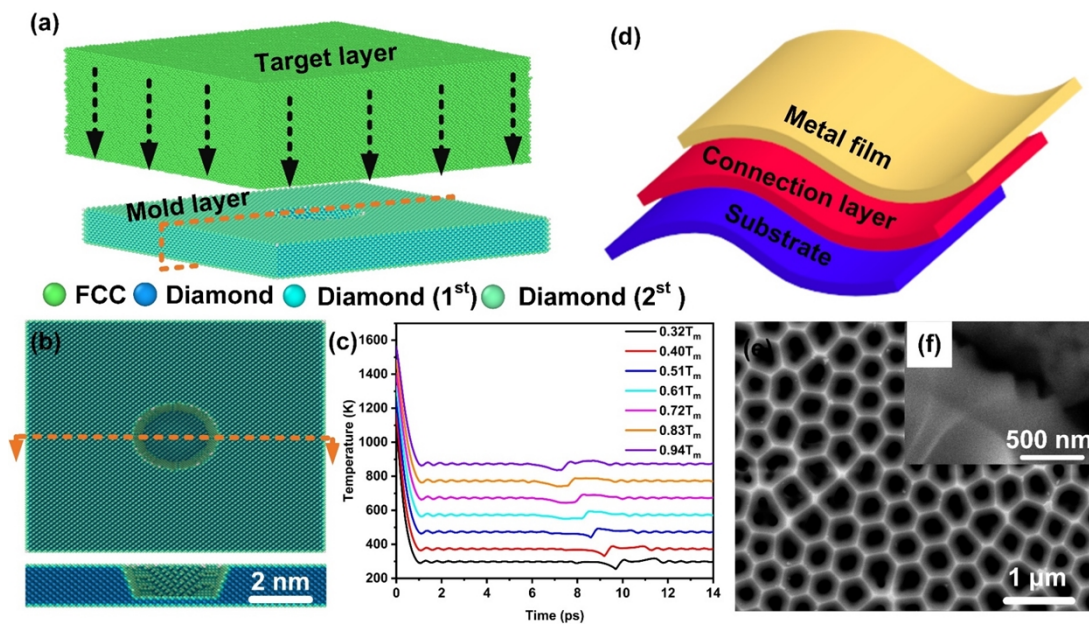
Supplementary Fig. S9 Experimental setup and MD models. (a) Global view of the MD model, (b) Top and side views of the mold marked by the dashed box in Fig. 1(a). (c) Temperature control curves, (d) Schematic diagram of the target material. (e) SEM image (top view) of the AAO mold, (f) SEM image (cross-sectional view) of the AAO mold.

Supplementary Table S1 [1–4] Material parameters.

Metal	b (nm)	T_m (K)	G (MPa)	E (MPa)	ρ_a (kg m^{-3})	k (J k^{-1})
Al	0.286	933	$29438.4-15.052T$	$100\exp(-6.67\times10^{-3}T)$	2700 (300 K)	1.38×10^{-23}
Ag	0.289	1235	$29997.5-12T-7.96\times10^{-5}T^2$	$62.69-5\times10^{-2}T$	10490 (300 K)	1.38×10^{-23}
Au	0.288	1337	28000 (300 K)	$121754.14-219.18T$	29162 (300 K)	1.38×10^{-23}

Supplementary Table S2 The L-J potential parameters.

Interaction Type	ε(eV)	σ (Å)
Al-Si	0.0195	3.9173
Au-Si	0.0772	3.2124
Ag-Si	0.0202	3.6421

Supplementary notes

1. Thermal-affected forming behaviors

The morphologies of the nanostructures were characterized by SEM and AFM. Fig. S1(a_1)-(a_3) present the SEM images of the Al nanostructures formed at 298 K, 773 K, and 873 K, respectively. According the AFM results shown in Fig. S1(b_1)-(b_3), the forming depth of the Al nanostructures formed at 298 K, 763 K, and 873 K, is 72.02 nm, 205.38 nm, and 103.2 nm, respectively. For the Ag nanostructures (Fig. S1(d_1)-(d_3)), the forming depth at 298 K, 673 K, and 873 K is 76.33 nm, 207.4 nm, and 121.5 nm, respectively. Additionally, it can be found from the 2D profiles of the nanostructures (Fig. S1(e_1) and (e_2)) that the nanostructures formed at 673 K showed a smoother surface and a sharper edge, which was consistent with SEM observations (Fig. S1(a_2)).

Fig. S2 shows the forming depth curves the Al and Ag nano-sheets. It can be found that the maximum forming depth of the Al and Ag nanostructures were both obtained at 673 K. The dynamic forming behavior of the nano-sheets under various processing temperatures was recorded and plotted in Fig. S3(a-c). It is worth noting that the dynamic forming of metal nanostructures discussed in this work refers to the forward deformation process, while the rebounds process and elastic recovery of the metal target are not considered. The time-step prior to the contact between the lower surface of the metal target and the upper surface of the mold was selected as the unified starting point of the dynamic deformation process. The time intervals of the dynamic forming process of Al, Au, and Ag nanostructures were set to 3 ps, 4 ps and 5 ps, respectively, due to the difference in the elastic modulus of the materials. Based on the dynamic forming curves, the dynamic forming of nano-sheets in laser shock forming process can be divided into three stages: elastic deformation (ED), plastic flow (PL), creep filling (CF). The PL stage showed the most significant contribution to the entire forming

process. As shown in Fig. S3(a-c), temperature had a positive effect on plastic flow behavior in the thermal-promoted formability stage, meaning that thermal expedited the material transfer process from the nano-sheet to the mold. This acceleration effect in the filling process weakened at 773 K, as evidenced by the orange curve in Fig. Fig. S3(a-c). To clearly reveal the influence of temperature on the atomic movement in laser shock forming processes, the trajectories of randomly selected Au atoms at processing temperatures of 298 K, 473 K, and 773 K were extracted (Fig. S3(d)-(f)). The CF (blue dotted box in Fig. S3(e)) occurred late in the filling process with an ultra-short time scale (0.5 ps-1 ps) accompanied by ultra-small-scale deformation (< 0.3 nm). In addition, the dynamic forming behavior of nano-metals in laser shock forming process was believed to be closely related to stress propagation states. The snapshots of dynamic stress propagation along the Z axis at 673 K are captured in Fig. S3(g)-(n). It can be seen that there is a uniaxial elastic wave transmission along the z-axis and a stress rebound process caused by the free surface (≤2.5 ps). The metal target suffered from the uniaxial ED and PL behaviors parallel to the Z-axis direction. When the time-step exceeds 2.5 ps, the additional constraint force provided by the mold (Fig. S3(j) and (k)) prevented the plastic deformation of the nanostructure and caused the CF behavior, which was consistent with the evolution of the forming depth in the dynamic deformation curves shown in Fig. S3(a-c).

2. Defect evolution in thermal-promoted formability stage

In the thermal-promoted formability stage, the dominant mechanism of plastic deformation was dislocation motion. We analyzed the dynamic dislocation density evolution by DXA to reveal the influence of temperature on the defect evolution. From Fig. S4, the rise in temperature increased the dislocation density in the Al and Ag nano-sheets (Fig. S4(a) and (c)). The accelerated proliferation of Shockley dislocations was the leading factor for the increase in dislocation density. On the other hand, the deterioration of metal plasticity caused

13

by dislocation reaction was concerned. The major dislocation hardening reactions in FCC-type metals includes Hirth and Stair-rod dislocations [5,6]. We calculated the density of reinforcing dislocation during the ultrahigh-strain-rate forming process in the thermal-promoted formability stage, and plotted in Fig. S6. It can be found that increasing temperature showed a slight effect on the frequency of dislocation reactions merely.

3. Defect evolution in thermal-weakened formability stage

In the thermal-weakened formability stage, the dominant mechanism of plastic deformation was the reversible phase transformation. We revealed the transformation of the deformation mechanism through the evolution of the dislocation density and phase volume fraction, as shown in Fig. S7 and Fig. S8. Excess thermal input led to an accelerated dislocation annihilation testifying by the dislocation length evolution curves in the thermal-weakened formability stage (Fig. S7). Also, significantly different phase transformation behavior was observed in the thermal-promoted formability and thermal-weakened formability stages (Fig. S8). The phase transformation in thermal-promoted formability stage can be summarized as limited FCC-BCC and increasing FCC-HCP change (Fig. S8(a)-(c)). However, the volume fraction of BCC phase (>20%) raised significantly in the thermal-weakened formability stage (Fig. S8(b)). When the rebound stress wave was activated (~3.5 ps), the plentiful metastable BCC phase transformed into FCC and HCP phases, as evidenced by the recovery of the FCC phase and the continuous increase of the HCP phase (Fig. S8(d) and (e)). The phase transformation behavior in the thermal-weakened formability stage can be summarized into three categories: FCC-HCP, FCC-BCC-HCP and FCC-BCC-FCC.

References

1   E. I. Galindo-Nava, J. Sietsma and P. E. J. Rivera-Díaz-Del-Castillo, *Acta Mater.*, 2012, **60**, 2615–2624.

2   G. P. Purja Pun and Y. Mishin, *Acta Mater.*, 2009, **57**, 5531–5542.

3   H. Xie, F. Yin, T. Yu, G. Lu and Y. Zhang, *Acta Mater.*, 2015, **85**, 191–198.

4   C. Birleanu, M. Pustan, V. Merie, R. Müller, R. Voicu, A. Baracu and S. Craciun, *IOP Conf. Ser. Mater. Sci. Eng.*, , DOI:10.1088/1757-899X/147/1/012021.

5   Y. Zhang, S. Jiang, X. Zhu and Y. Zhao, *Phys. E Low-Dimensional Syst. Nanostructures*, 2017, **90**, 90–97.

6   A. Kardani and A. Montazeri, *Comput. Mater. Sci.*, 2018, **152**, 381–392.